The Astrophysical Journal, 864:98 (15pp), 2018 September 1 https://doi.org/10.3847/1538-4357/aad4a7
© 2018. The American Astronomical Society. All rights reserved.

Dissection of the Collisional and Collisionless Mass Components in a Mini Sample of CLASH and HFF Massive Galaxy Clusters at $z \approx 0.4$

M. Bonamigo[1], C. Grillo[1,2], S. Ettori[3,4], G. B. Caminha[5,6], P. Rosati[6], A. Mercurio[7], E. Munari[8], M. Annunziatella[8,9], I. Balestra[10], and M. Lombardi[2]

[1] Dark Cosmology Centre, Niels Bohr Institute, University of Copenhagen, Juliane Maries Vej 30, DK-2100 Copenhagen, Denmark; bonamigo@dark-cosmology.dk
[2] Dipartimento di Fisica, Università degli Studi di Milano, via Celoria 16, I-20133 Milano, Italy
[3] INAF, Osservatorio Astronomico di Bologna, Via Piero Gobetti, 93/3, I-40129 Bologna, Italy
[4] INFN, Sezione di Bologna, viale Berti Pichat 6/2, I-40127 Bologna, Italy
[5] Kapteyn Astronomical Institute, University of Groningen, P.O. Box 800, 9700 AV, Groningen, The Netherlands
[6] Dipartimento di Fisica e Scienze della Terra, Università degli Studi di Ferrara, Via Saragat 1, I-44122 Ferrara, Italy
[7] INAF—Osservatorio Astronomico di Capodimonte, Via Moiariello 16, I-80131 Napoli, Italy
[8] INAF—Osservatorio Astronomico di Trieste, Via G.B. Tiepolo, 11 I-34143 Trieste, Italy
[9] Department of Physics and Astronomy, Tufts University, 574 Boston Avenue, Medford, MA 02155, USA
[10] University Observatory Munich, Scheinerstrasse 1, D-81679 Munich, Germany

Received 2017 December 11; revised 2018 July 15; accepted 2018 July 17; published 2018 September 4

Abstract

We present a multiwavelength study of the massive ($M_{200c} \approx (1–2) \times 10^{15} M_{\odot}$) galaxy clusters RXC J2248.7−4431, MACS J0416.1−2403, and MACS J1206.2−0847 at $z \approx 0.4$. Using the X-ray surface brightness of the clusters from the deep *Chandra* data to model their hot gas, we are able to disentangle this mass term from the diffuse dark matter (DM) in our new strong-lensing analysis, with approximately 50–100 secure multiple images per cluster, effectively separating the collisional and collisionless mass components of the clusters. At a radial distance of 10% of R_{200c} (approximately 200 kpc), we measure a projected total mass of (0.129 ± 0.001), (0.131 ± 0.001) and $(0.137 \pm 0.001) \times M_{200c}$, for RXC J2248, MACS J0416 and MACS J1206, respectively. These values are surprisingly similar considering the large differences in the merging configurations and, consequently, in the mass models of the clusters. Interestingly, at the same radii, the hot gas over total mass fractions differ substantially, ranging from 0.082 ± 0.001 to 0.133 ± 0.001, which reflects the various dynamical states of the clusters. Moreover, we do not find a statistically significant offset between the positions of the peak of the diffuse DM component and of the BCG in the more complex clusters of the sample. We extend the previous findings of a number of massive sub-halos that are higher than in numerical simulations to this sample of clusters. Our results highlight the importance of a proper separation of the different mass components to study the properties of DM in galaxy clusters in detail.

Key words: dark matter – galaxies: clusters: individual (RXC J2248.7-4431, MACS J0416.1-2403, MACS J1206.2-0847) – gravitational lensing: strong – X-rays: galaxies: clusters

1. Introduction

In recent years, many observational campaigns have targeted massive galaxy clusters to study and model their gravitational lensing of background sources. While some surveys—such as the Cluster Lensing And Supernova survey with Hubble (CLASH; Postman et al. 2012)—have focused on the investigation of the dark matter (DM) halos in which these clusters live, others—such as the Hubble Frontier Fields (HFF; Lotz et al. 2017) and the Reionization Lensing Cluster Survey (Salmon et al. 2017)—have turned clusters into powerful gravitational telescopes to explore the high-z universe. New imminent surveys (i.e., BUFFALO; P.I. Steinhardt, C.) are planning to expand this field even further and several GTO programs of the coming *James Webb Space Telescope* have already been scheduled to the study of lensing galaxy clusters. Ground-based photometric and spectroscopic data have been used to complement the space-based observations. For instance, within the CLASH-VLT program (Rosati et al. 2014), thousands of member galaxies and lensed multiple images have been spectroscopically confirmed (e.g., Biviano et al. 2013; Balestra et al. 2016; Monna et al. 2017). In the cores of clusters, the Multi Unit Spectroscopic Explorer (MUSE; Bacon et al. 2012) at the VLT has also allowed for the serendipitous discovery of lensed systems that are not detected in the *HST* images (Richard et al. 2015; Caminha et al. 2017b; Karman et al. 2017; Mahler et al. 2018), in addition to the redshift measurement of previously known objects. Moreover, the same massive galaxy clusters have also been the targets of numerous observations with X-ray telescopes, such as *Chandra* and *XMM Newton*, and submillimeter and radio antennas, which have characterized with extreme precision the hot intracluster gas component (e.g., Donahue et al. 2014; Ogrean et al. 2016; Rumsey et al. 2016; van Weeren et al. 2017).

All of these studies have helped to create a multiwavelength view of galaxy clusters. Multiprobe analyses have the advantage of highlighting systematic errors (or the lack thereof; see e.g., Balestra et al. 2013), breaking degeneracies (i.e., line-of-sight projection; see e.g., Morandi et al. 2012; Umetsu et al. 2015; Sereno et al. 2017), and separating the cluster components (i.e., diffuse DM, hot intracluster gas and cluster-member galaxies; see e.g., Annunziatella et al. 2018). This paper aims to separate the cluster component. Following Bonamigo et al. (2017), we combine information from gravitational lensing and X-ray observations to isolate the different mass components in a small sample of galaxy clusters: RXC J2248.7−4431, MACS J0416.1−2403, and MACS J1206.2−0847. This mass dissection allows for a more direct comparison with numerical simulations and theoretical predictions because the reconstructed mass components with different characteristics (i.e., different physical properties and spatial distributions) are less contaminated with each

other. An unbiased characterization of the cluster components can shed light on the nature of DM (i.e., the Bullet cluster, 1E 0657 −56; Clowe et al. 2006) and can be used to measure the values of the cosmological parameters. For example, the shape of the mass density profile is related to the cluster formation history and the value of the DM cross-section through the density profile characteristic radius (Wechsler et al. 2002; Zhao et al. 2003) and inner slope (Firmani et al. 2000; Spergel & Steinhardt 2000; Macciò et al. 2012; Vogelsberger et al. 2012). Similarly, self-interacting DM can produce an offset between the center of its mass distribution and the truly collisionless galaxy distribution in a cluster. Moreover, the fraction of baryons in galaxy clusters can be used to infer the background value, the cosmological baryon fraction Ω_b (White et al. 1993; Evrard 1997; Ettori et al. 2003; Allen et al. 2008; Planelles et al. 2013).

The rest of this paper is organized as follows. In Section 2, we briefly summarize the technique used to separate the cluster mass components in our analysis. Then, in Section 3, we introduce the studied sample of galaxy clusters. Section 4 contains the results of the X-ray surface brightness and strong-lensing analyses, on an individual cluster basis. Meanwhile, in Section 5, we compare the results across the whole sample. Finally, in Section 6, we summarize our conclusions.

Throughout this paper, we adopt a flat ΛCDM cosmology with Hubble constant $H_0 = 70$ km s^{-1} Mpc^{-1} and total matter density $\Omega_m = 0.3$. All magnitudes are given in the AB system.

2. Method

The method that we adopt to separate the different cluster mass components consists of two steps: first, we fit the X-ray surface brightness to obtain a mass model of the hot intracluster gas; then, we include this in the strong-lensing analysis as a fixed component, to derive the DM and member galaxy mass distributions.

In the following subsections, we will briefly summarize these two steps; a more detailed presentation of the method can be found in Bonamigo et al. (2017).

2.1. X-Ray

We choose to describe the mass distribution of the hot intracluster gas with a combination of several dual Pseudo-Isothermal Ellipsoidal (Elíasdóttir et al. 2007; Suyu & Halkola 2010, dPIE) distributions because this profile is already available in most gravitational lensing software. To convert the gas mass density into its corresponding X-ray surface brightness, we compute the cooling function, which gives the number of emitted photons per unit of volume. In the energy range that is considered in this work (0.7–2 keV), the dependence of the cooling function on the values of the gas temperature and metallicity is very weak (Ettori 2000). Therefore, we can safely adopt constant values for these quantities throughout the whole observed region of a cluster. Within these assumptions, the X-ray surface brightness is proportional, via the cooling function, to the the squared mass density projected along the line of sight.

From the median values of the gas temperature and metallicity, which are derived from the measured radial profiles, we compute the cooling function using the Astrophysical Plasma Emission Code model.[11] We then measure the background emission from an image region at a projected distance of more than 1.5 Mpc from the cluster center and use a photoelectric absorption (phabs)[12] model for the foreground galactic gas. Finally, we fit the *Chandra* image, reduced and corrected for exposure, using the *Sherpa* application.[13]

2.2. Strong Lensing

After creating a model for the hot intracluster gas mass, we proceed to include it in the cluster strong-lensing analysis. As detailed in Bonamigo et al. (2017), we have included the hot gas term as a fixed component. This is justified by the small set of assumptions that are required to derive the hot gas mass density profiles from the X-ray surface brightness and by the fact that the statistical errors on the inferred hot gas mass density profiles are smaller than those typically associated with the other cluster mass components. The model of the cluster total mass consists of three components: large-scale DM halos, the hot intracluster gas, and galaxy-scale halos. The first term describes the diffuse DM that spans the whole cluster and accounts for most of its total mass. For this component, we use one or more Pseudo-Isothermal Elliptical Mass Distribution (hereafter PIEMD; Kassiola & Kovner 1993) profiles, the number of the profiles depending on the degree of complexity of the cluster mass distribution. Each PIEMD profile has six free parameters: center position, x_h and y_h, ellipticity, ϵ_h, position angle, θ_h, core radius, $R_{C,h}$, and central velocity dispersion, $\sigma_{0,h}$. The galaxy-scale halos are modeled instead with spherical dPIE distributions, with their centers fixed on the luminosity centers of the cluster galaxies, thus resulting in two free parameters for each galaxy: truncation radius $R_{T,i}$ and central velocity dispersion $\sigma_{0,i}$. To reduce the otherwise too large number of free parameters, we scale the values of $R_{T,i}$ and $\sigma_{0,i}$ depending on L_i (i.e., the galaxy luminosity in the *HST*/WFC3 filter F160W) with respect to a reference luminosity, L_g, so that $R_{T,i} = R_{T,g}(L_i/L_g)^{0.5}$ and $\sigma_{0,i} = \sigma_{0,g}(L_i/L_g)^{0.35}$. With these scaling relations, which reproduce the tilt of the fundamental plane of elliptical galaxies (Faber et al. 1987; Bender et al. 1992), all of the galaxy-scale halos are parametrized by only two quantities: $\sigma_{0,g}$ and $R_{T,g}$.

To infer the values of all the model parameters of the mass components of a cluster, we use the *lenstool* lensing software package (Jullo et al. 2007). We run an initial optimization on the positions of several tens of multiple images with positional errors of $0\farcs5$ and $1''$, respectively, for images detected on the *HST*- or MUSE-only data. Then, we multiply these errors by a constant factor, which is obtained by requiring that the best-fit χ^2 value is approximately equal to the number of degrees of freedom (d.o.f.) of the model (see Appendix B for further quantitative discussion on the implications of this assumption). Finally, we use the updated values of the positional errors to sample the posterior distribution of the cluster model parameters. By doing so, we make sure not to under- or over-estimate the uncertainties on the model parameters and to include possible systematic effects, such as line-of-sight mass components or unresolved substructures. A recent work by Acebron et al. (2017) has shown that an underestimated value for the positional error can lead to biased analyses and that the bias decreases when the χ^2 value is close to the number of d.o.f.

[11] http://atomdb.org/

[12] Xspec manual: phabs

[13] http://cxc.harvard.edu/sherpa

3. The Sample

The sample that we studied in this work is composed of three galaxy clusters: RXC J2248.7−4431 (also known as Abell S1063), MACS J0416.1−2403, and MACS J1206.2−0847. Hereafter, we will use the shortened names RXC J2248, MACS J0416, and MACS J1206, respectively. For these objects, some of the best state-of-the-art observations are available: multiband *HST* imaging, VLT/MUSE and VIMOS spectroscopic data, and deep *Chandra* observations. Indeed, thanks to the CLASH-VLT program (Rosati et al. 2014), spectra for a large number of sources are available, on the order of thousands per cluster field. Moreover, all three targets have been observed for several hours with the MUSE integral-field spectrograph: two pointings of 3.1 and 4.8 hr each in RXC J2248 (ID 060.A-9345 (A) and 095.A-0653(A), P.I.: K. Caputi), two pointings of 2 and 11 hr in MACS J0416 (ID 094.A-0115(B), P.I.: J. Richard, and ID 094.A-0525(A) P.I.: F.E. Bauer), and three pointings of about 4 hr in MACS J1206 (ID 095.A-0181(A) and 097.A-0269(A), P.I.: J. Richard). Additionally, two of the galaxy clusters, RXC J2248 and MACS J0416, are also part of the HFF sample (Lotz et al. 2017). These datasets make these clusters the ideal candidates for accurate strong-lensing analyses (Caminha et al. 2016, 2017a, 2017b; Grillo et al. 2016; Lagattuta et al. 2017), which can be used as the foundation for the multi-wavelength analysis that we perform in this work.

To build a precise model of the hot intracluster gas, we use deep *Chandra* observations. The combined exposure times are 123 ks (obsID 4966, 18611 and 18818), 293 ks (obsID 16236, 16237, 16304, 16523, 17313) and 23 ks (obsID 3277), for RXC J2248, MACS J0416 and MACS J1206, respectively. A detailed X-ray analysis of MACS0416 is given in Ogrean et al. (2016). All of the images are reduced with the software *CIAO* application (version 4.7+), using the *CALDB* calibration database (version 4.6.8+). The resolution of the surface brightness maps, limited to the energy range from 0.7 to 2 keV, is scaled down to a pixel size of 1.″968 (3.″936 for MACSJ 0416). This pixel size is much larger than *Chandra*'s on-axis point-spread function; therefore, we do not consider this effect in our analysis.

Accurate strong-lensing models rely on highly complete and pure cluster-member catalogs and samples of secure multiple images that cover a broad range of redshifts. By combining the information from the *HST*, VIMOS and MUSE data, we are able to produce such catalogs. In particular, we start from the spectroscopically confirmed cluster members to define a color-space region, which we then use to derive the probability of a galaxy to belong to the cluster (Grillo et al. 2015). The resulting catalogs of cluster members have a completeness value of approximately 95% (Grillo et al. 2015; Caminha et al. 2017b) and are mostly comprised of spectroscopically confirmed members. Conversely, the multiple-image catalogs consist only of secure spectroscopically confirmed sources (Balestra et al. 2016; Caminha et al. 2016, 2017b).

The galaxy cluster RXC J2248, which was first identified as Abell S1063 by Abell et al. (1989), is the most massive,[14] $M_{200c} = (2.03 \pm 0.67) \times 10^{15} M_{\odot}$ (Umetsu et al. 2014), and the nearest in the sample; at its redshift, 0.348, 1″ corresponds to 4.92 kpc. It is also the least complex, with an almost unimodal total mass distribution and a single BCG (R.A. = 22:48:43.970 and decl. = −44:31:51.16). The X-ray surface brightness is quite symmetric, although it is slightly offset from cluster center, and it shows a cool core, that instead coincides with the position of the BCG. In total, we use 55 multiple images (all spectroscopically confirmed) from 20 background sources, covering a redshift range from 0.73 to 6.11 (extending the sample by Karman et al. 2017). We describe the total mass distribution of RXC J2248 with a model, similar to that presented in Caminha et al. (2016), which consists of a large-scale elliptical PIEMD halo (DM and intracluster light), three elliptical dPIE components (hot gas), 222 galaxy-scale dPIE halos (member galaxies), and an additional small-scale spherical halo. The latter was initially centered on the location of a small group of galaxies but, in the final optimized model, its position does not coincide with any particular feature of the cluster. This additional component reduces the offset between the observed and model-predicted positions of some multiple images in the north–east region and it has also been introduced in the model of RXC J2248 by Kawamata et al. (2018). It is assumed to have a spherical singular isothermal density profile with three free parameters: center position, x_{h2} and y_{h2}, and central velocity dispersion, $\sigma_{0,h2}$. The reference galaxy for the cluster-member scaling relations is the BCG.

MACS J0416 is a merging cluster, with a M_{200c} mass value of approximately $(1.04 \pm 0.22) \times 10^{15} M_{\odot}$ (Umetsu et al. 2014), and located at a redshift of 0.396, where 1″ corresponds to 5.34 kpc. It was first discovered in the Massive Cluster Survey (MACS) by Mann & Ebeling (2012). It hosts two BCGs, G1 and G2, located, respectively, in the northeast (R.A. = 04:16:09.154 and decl. = −24:04:02.90) and southwest (R.A. = 04:16:07.671 and decl. = −24:04:38.75) regions of the cluster. Its merging status is evident from the X-ray emission morphology and the large projected separation (∼200 kpc) between the two BCGs. In the strong-lensing analysis, we use 102 spectroscopically confirmed multiple images from 37 background sources, with redshifts from 0.94 to 6.15 (Caminha et al. 2017a). The mass model is an update of the model used in Bonamigo et al. (2017) (itself derived from Grillo et al. 2015; Caminha et al. 2017a) and consists of three large-scale PIEMD halos (DM and intracluster light), four elliptical dPIE components (hot gas), and 193 galaxy-scale dPIE halos (member galaxies, including the two BCGs). Two of the large-scale halos are elliptical in projection and describe the two merging subclusters, while the third component traces the mass of a small group of galaxies present in the north–east region of the cluster. This halo is assumed to be spherical with four free parameters: center position, x_{h3} and y_{h3}, core radius, $R_{C,h3}$, and central velocity dispersion, $\sigma_{0,h3}$. Moreover, we use the northern BCG, G1, as the reference galaxy for the scaling relations that define the properties of the cluster-member galaxies. Finally, an additional galaxy-scale mass component takes into account the lensing perturbation introduced by a foreground galaxy (R.A. = 04:16:06.82 and decl. = −24:05:08.4) at redshift 0.112. This galaxy is described by a dPIE profile at the redshift of the cluster and, therefore, the values of σ_0 and R_T should be considered only as effective parameters. As shown by Chirivì et al. (2018), the introduction of this foreground galaxy at the cluster redshift gives results that are very similar to a full multiplane analysis, both in terms of the inferred cluster parameter values and offset between the observed and model-predicted positions of the multiple images.

Finally, the galaxy cluster MACS J1206 has a M_{200c} mass value of approximately $(1.59 \pm 0.36) \times 10^{15} M_{\odot}$ (Umetsu

[14] The mass M_{200c} is defined as the mass within a sphere inside which the value of the mean density is equal to 200 times that of the universe critical density at each cluster redshift.

Table 1
Summary of Cluster Properties and Lensing Data

Cluster	z	M_{200c} ($10^{15}M_{\odot}$)	R_{200c} (Mpc)	N_{mem}	N_{im}
RXC J2248	0.348	2.03 ± 0.67	2.32 ± 0.26	222	55
MACS J0416	0.396	1.04 ± 0.22	1.82 ± 0.13	193	102
MACS J1206	0.439	1.59 ± 0.36	2.06 ± 0.16	265	82

Note. For each cluster, we report the redshift, z, total mass, M_{200c}, Radius, R_{200c}, number of member galaxy, N_{mem}, and number of secure multiple images, N_{im}, all spectroscopically confirmed.

et al. 2014), and it is located at a redshift of 0.439; at this distance, 1″ corresponds to 5.68 kpc. It was discovered in the *ROSAT* All-Sky Survey (RXC J1206.2−0848; Böhringer et al. 2001). Even though the cluster appears as a relaxed object (Zitrin et al. 2012; Biviano et al. 2013), both the X-ray surface brightness and the total mass show asymmetric distributions that are characterized by a single peak located approximately at the BCG position (R.A. = 12:06:12.149 and decl. = −8:48:03.37). The multiple-image catalog consists of 82 images (all spectroscopically confirmed) from 27 background sources that span a redshift range from 1.01 to 6.06 (Caminha et al. 2017b). Remarkably, 11 of these images are in the central 50 kpc, allowing for a very accurate measurement of the mass distribution in the core of the cluster. The total mass model is similar to that by Caminha et al. (2017b) and consists of three large-scale elliptical halos (DM and intracluster light), three elliptical dPIE components (hot gas) and 265 galaxy-scale dPIE halos (member galaxies) and an external shear. The large-scale elliptical halos are needed to mimic the asymmetric total mass distribution of the cluster and they should not be considered as separate subclusters. We choose the luminosity value of the BCG as a reference in the scaling relations of the cluster members.

In Table 1, we summarize the most important information for each cluster, for the lensing and for the following analysis.

4. Results

The exquisite quality of the multiwavelength data that was presented in the previous section allows us to create very accurate models of the total mass distribution of the galaxy clusters in the sample. Here, we present these models. We will only discuss the full models that include both the DM and hot gas components. As noted in Bonamigo et al. (2017), traditional methods cannot determine the model parameters of the DM-only components because they are not separated from the hot gas term, which can only be subtracted a-posteriori. We refer to Bonamigo et al. (2017) for a more detailed comparison with traditional techniques.

We measure the cluster temperature and metallicity by taking the median values of their radial profiles. These have been derived from the X-ray spectra up to a distance from the cluster center of 1.′5, 4.′0, and 3.′0, for RXC J2248, MACS J0416 and MACS J1206, respectively. The adopted values of temperature (metallicity) are 12.8 (0.31), 10.4 (0.25), and 13.0 KeV (0.22). To describe the hot gas mass of the clusters, we fit the X-ray surface brightness with three elliptical dPIE profiles (four in the case of MACS J0416) plus uniform backgrounds of 0.11, 0.89 and 0.02 counts/pixel, measured from the *Chandra* images by masking a circular region of radius of approximately 1.5 Mpc around each cluster center. The resulting minimum values of the Cash statistic C, used for the fit, are 13794.8 (11551 d.o.f), 3438.5 (2828 d.o.f), and 9785.9 (11589 d.o.f), for RXC J2248, MACS J0416 and MACS J1206, respectively. Additionally, we have tried alternative models, which we discuss in Appendix A. Figure 1 shows the X-ray surface brightness of the three clusters, one for each row. The first two columns show the logarithm of the observed data, S_X^{obs}, and best-fit model, S_X^{mod}, respectively. The images in the third column are the relative difference between the data and the model. Only circular apertures of radius 120″ are shown, which correspond to those considered when fitting the cluster X-ray surface brightness. From these plots, it is clear that the complex geometry of the X-ray surface brightness requires multiple components to describe either individual subclusters, such as in MACS J0416, or the asymmetry of the emission, such as in MACS J1206. We note that in this work we provide an updated model of the hot intracluster gas in MACS J0416 presented in Bonamigo et al. (2017). While the previous spherical-component approximation provides a good fit to the data, the new elliptical model is favored by several model-selection criteria, such as the Akaike information criterion (AIC, Akaike 1974) and Bayesian Information Criterion (BIC, Schwarz 1978), and it is a more accurate representation the complex nature of this cluster. The median values and confidence level (CL) (68%) uncertainties of the mass density parameters of the intracluster gas are presented in Tables 2–4. The positions of the centers refer to the BCGs of the clusters (G1 for MACS J0416).

The next step in the analysis is to include these hot gas models as fixed mass components in the strong-lensing analysis. We use a first optimization of the lensing model of each cluster to derive new values for the error in the positions of the multiple images. These are 0.″46, 0.″57 and 0.″35, for RXC J2248, MACS J0416 and MACS J1206, respectively. The subsequent best-fit models have values of the minimum-χ^2 of 59.71 (59 d.o.f), 111.0 (110 d.o.f) and 90.9 (88 d.o.f); the corresponding values of the rms of the multiple-image position offsets are 0.″48, 0.″59 and 0.″45 (median values 0.″37, 0.″40 and 0.″36). Tables 5–7 contain the inferred values of the mass model parameters.[15] Here, we quote the median values and the 68%, 95% and 99.7% CL intervals.

The surface mass densities of the different cluster components are shown in Figure 2 (left-hand panel), where they are represented as isocontours overlaid on color-composite *HST* WCF3/ACS images of the clusters. The total (white) and DM (blue) isodensity contours are drawn at 3.5, 7.2, 15 and 30 in units of $10^{-4}\ M_{\odot}\ \mathrm{kpc}^{-2}$; while the gas (red) isodensity contours are drawn at 0.65, 1.0, 1.6 and 2.5 in units of $10^{-4}\ M_{\odot}\ \mathrm{kpc}^{-2}$. The right-hand panel of Figure 2 shows a zoom-in of the central region of the images on the left. The positions of the BCGs are shown with green plus signs, that are 2″ of width. The blue contours in the right-hand panel show the position of the diffuse DM component density peak with 1σ, 2σ and 3σ CLs. From these plots, the need for a full component separation is clear: the DM and hot-gas mass distributions have different shapes and centers, due to their intrinsically different physical properties. For example, while the DM component in RXC J2248 is roughly centered on the BCG, the hot-gas mass distribution is skewed toward northeast. In MACS J1206, this

[15] The *lenstool* input files and sampled posterior distributions can be found at https://sites.google.com/site/vltclashpublic/.

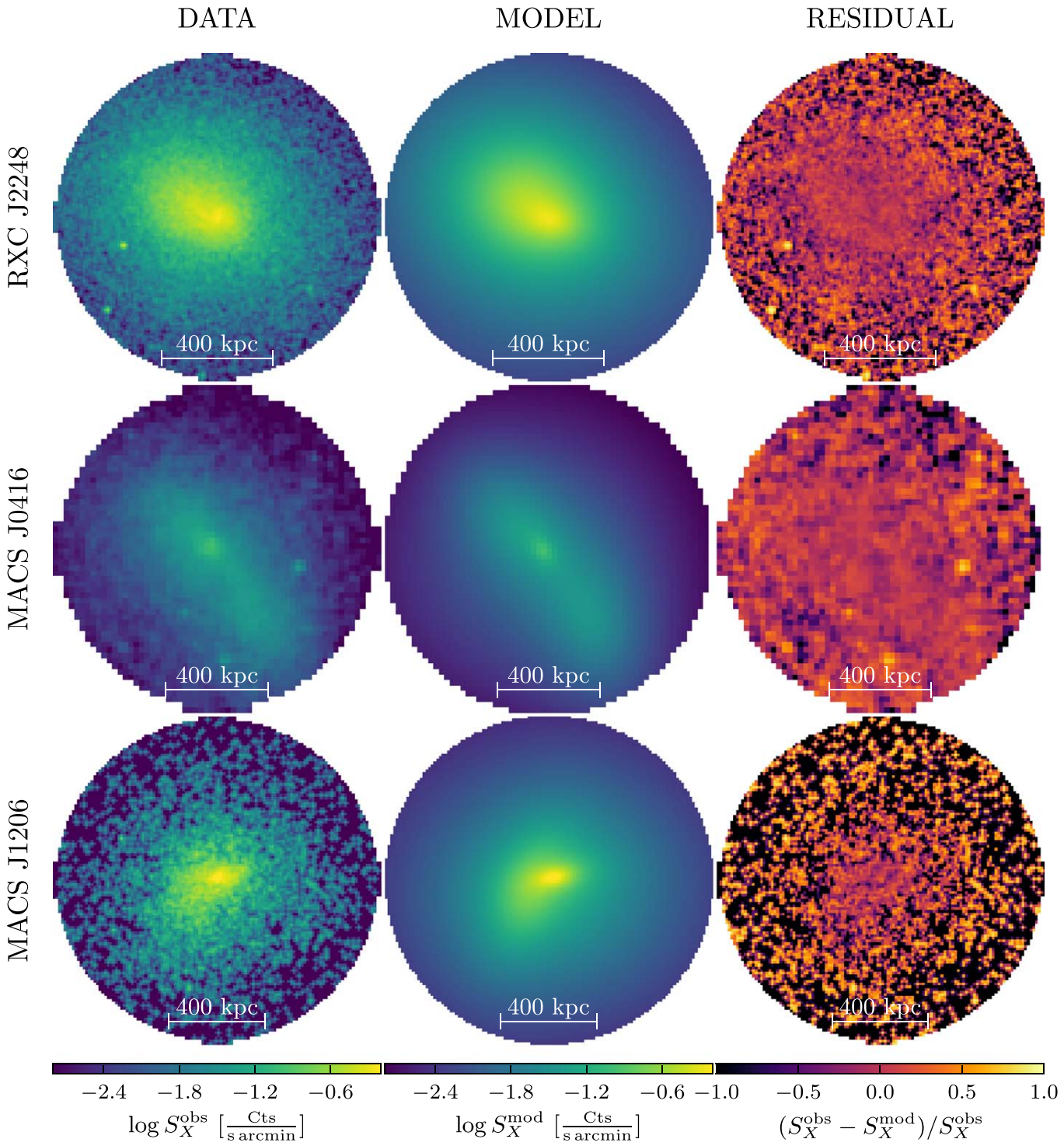

Figure 1. X-ray surface brightness (logarithmic scale) and relative residual maps: data (first column), best-fitting model (second column) and relative residuals (third column). The rows represent, from top to bottom, the clusters RXC J2248, MACS J0416 and MACS J1206. Each panel shows the circular aperture of radius of 120″ used in the fitting procedure. The point sources are shown only for graphical reasons and they have been masked out in the fitting procedure.

latter component is elongated toward the southeast region of the cluster, creating a twist in the isodensity contours; such feature is not present in the DM mass distribution, which, however, tends to be fairly lopsided. In all clusters, especially in RXC J2248, the hot-gas component is rounder than the DM one; in MACS J0416, this happens a-symmetrically, with the northeast region being rounder than the southeast one. Moreover, with the exception of RXC J2248, we find that the peaks of the density of the diffuse DM components are consistent, within 3σ, with the positions of the BCGs. Indeed, the distances between the BCGs and the DM component density peaks are $(9.3^{+1.7}_{-1.7})$, $(13.8^{+4.7}_{-5.3})$, and $(3.9^{+1.0}_{-0.8})$ kpc, for

Table 2
RXC J2248: Median Values and Confidence Level (68%) Uncertainties of the Three-component dPIE Model of the X-Ray Surface Brightness

	Comp. 1	Comp. 2	Comp. 3
x_0 ($''$)	27^{+22}_{-21}	$-18.2^{+0.6}_{-0.7}$	$0.2^{+0.4}_{-0.4}$
y_0 ($''$)	-70^{+8}_{-15}	$13.6^{+0.5}_{-0.5}$	$-1.2^{+0.3}_{-0.2}$
ϵ	$0.71^{+0.12}_{-0.17}$	$0.13^{+0.01}_{-0.01}$	$0.34^{+0.02}_{-0.03}$
θ (degree)	-163^{+8}_{-7}	-29^{+3}_{-2}	-15^{+2}_{-2}
R_C ($''$)	$188.6^{+0.1}_{-0.1}$	$36.0^{+0.5}_{-0.6}$	$14.6^{+0.3}_{-0.5}$
R_T ($''$)	$189.1^{+0.1}_{-0.1}$	360^{+50}_{-50}	359^{+4}_{-5}
σ_0 (km s^{-1})	440^{+20}_{-30}	539^{+6}_{-5}	308^{+7}_{-7}

Note. The center position refers to the BCG (R.A. = 22:48:43.970 and decl. = −44:31:51.16).

Table 3
MACS J0416: Median Values and Confidence Level (68%) Uncertainties of the Four-component dPIE Model of the X-Ray Surface Brightness

	Comp. 1	Comp. 2	Comp. 3	Comp. 4
x_0 ($''$)	$-19.6^{+2.2}_{-1.4}$	$30.7^{+0.5}_{-0.7}$	$-2.3^{+0.1}_{-0.1}$	$-20.2^{+0.2}_{-0.1}$
y_0 ($''$)	$-13.2^{+1.4}_{-1.1}$	$-48.7^{+0.3}_{-0.2}$	$-1^{+0.1}_{-0.1}$	$14.6^{+0.6}_{-0.4}$
ϵ	$0.09^{+0.05}_{-0.04}$	$0.41^{+0.03}_{-0.03}$	$0.42^{+0.04}_{-0.12}$	$0.39^{+0.03}_{-0.02}$
θ (degree)	-160^{+10}_{-20}	-71^{+2}_{-3}	-52^{+5}_{-6}	-47^{+3}_{-2}
R_C ($''$)	$149.3^{+0.1}_{-0.1}$	$34.8^{+0.5}_{-0.8}$	$10.3^{+0.7}_{-0.8}$	$50.8^{+0.9}_{-0.9}$
R_T ($''$)	$149.8^{+0.1}_{-0.1}$	160^{+20}_{-10}	24.20^{+7}_{-5}	$52.3^{+0.1}_{-0.1}$
σ_0 (km s^{-1})	529^{+4}_{-2}	306^{+3}_{-4}	134^{+6}_{-5}	346^{+4}_{-6}

Note. The center position refers to the northeast BCG, G1 (R.A. = 04:16:09.154 and decl. = −24:04:02.90).

Table 4
MACS J1206: Median Values and Confidence Level (68%) Uncertainties of the Three-component dPIE Model of the X-Ray Surface Brightness

	Comp. 1	Comp. 2	Comp. 3
x_0 ($''$)	$1.7^{+1.5}_{-0.9}$	$-13.9^{+1.5}_{-1.8}$	$3.3^{+0.7}_{-0.5}$
y_0 ($''$)	$-6.7^{+1.5}_{-1.3}$	$-7.6^{+1.4}_{-1.1}$	$2.1^{+0.4}_{-0.1}$
ϵ	$0.13^{+0.03}_{-0.06}$	$0.50^{+0.07}_{-0.03}$	$0.55^{+0.06}_{-0.04}$
θ (degree)	0^{+8}_{-10}	-111^{+4}_{-5}	-169^{+5}_{-2}
R_C ($''$)	59^{+5}_{-2}	39^{+3}_{-2}	$8.3^{+0.4}_{-0.8}$
R_T ($''$)	810^{+180}_{-400}	$43.9^{+0.1}_{-0.1}$	200^{+20}_{-110}
σ_0 (km s^{-1})	536^{+15}_{-6}	397^{+22}_{-8}	239^{+5}_{-13}

Note. The center position refers to the BCG (R.A. = 12:06:12.149 and decl. = −8:48:03.37).

RXC J2248, MACS J0416 and MACS J1206, respectively. We note that RXC J2248 is described by the simplest DM mass model and that the DM component seems to counterbalance the asymmetric hot gas component, which is skewed in the opposite direction.

From the previous maps, we obtain the radial profiles shown in Figure 3. The left-hand and right-hand panels contain, respectively, the surface mass density and cumulative projected mass profiles; each color corresponds to a different mass component: cluster members (green), hot intracluster gas (red), DM (blue), and total (black). The thin lines represent a subsample of the models extracted from the sampling of the posterior distribution, while the solid and dashed lines show their median and 16th–84th percentiles, respectively.

Table 5
RXC J2248: Median Values and Confidence Level (CL) Uncertainties for the Strong-lensing Model Parameters

	Median	68% CL	95% CL	99.7% CL
x_{h1} ($''$)	1.8	$^{+0.3}_{-0.3}$	$^{+0.6}_{-0.6}$	$^{+1.0}_{-0.8}$
y_{h1} ($''$)	−1.0	$^{+0.2}_{-0.2}$	$^{+0.4}_{-0.5}$	$^{+0.6}_{-0.7}$
ϵ_{h1}	0.64	$^{+0.01}_{-0.01}$	$^{+0.02}_{-0.01}$	$^{+0.03}_{-0.02}$
θ_{h1} (degree)	−38.7	$^{+0.3}_{-0.3}$	$^{+0.5}_{-0.5}$	$^{+0.7}_{-0.8}$
$R_{C,h1}$ ($''$)	19.2	$^{+0.7}_{-0.6}$	$^{+1.3}_{-1.3}$	$^{+2.0}_{-1.9}$
$\sigma_{0,h1}$ (km s^{-1})	1396	$^{+15}_{-17}$	$^{+27}_{-35}$	$^{+38}_{-53}$
x_{h2} ($''$)	−53.3	$^{+4.8}_{-6.0}$	$^{+8.8}_{-12.8}$	$^{+12.0}_{-21.4}$
y_{h2} ($''$)	27.1	$^{+2.8}_{-2.5}$	$^{+6.3}_{-4.8}$	$^{+10.9}_{-7.1}$
$\sigma_{0,h2}$ (km s^{-1})	282	$^{+35}_{-31}$	$^{+74}_{-60}$	$^{+118}_{-86}$
$R_{T,g}$ ($''$)	46.6	$^{+17.8}_{-13.8}$	$^{+42.0}_{-25.1}$	$^{+72.8}_{-33.7}$
$\sigma_{0,g}$ (km s^{-1})	274	$^{+16}_{-16}$	$^{+32}_{-33}$	$^{+53}_{-51}$

Note. The center position refers to the BCG (R.A. = 22:48:43.970 and decl. = −44:31:51.16). The angle θ_{h1} is measured counterclockwise from the west axis.

Table 6
MACS J0416: Median Values and Confidence Level (CL) Uncertainties for the Strong-lensing Model Parameters

	Median	68% CL	95% CL	99.7% CL
x_{h1} ($''$)	−2.5	$^{+0.9}_{-0.8}$	$^{+1.8}_{-1.4}$	$^{+2.8}_{-1.9}$
y_{h1} ($''$)	1.8	$^{+0.5}_{-0.6}$	$^{+0.9}_{-1.2}$	$^{+1.3}_{-2.0}$
ϵ_{h1}	0.86	$^{+0.01}_{-0.01}$	$^{+0.03}_{-0.03}$	$^{+0.04}_{-0.06}$
θ_{h1} (degree)	145.2	$^{+0.7}_{-0.9}$	$^{+1.5}_{-1.9}$	$^{+2.6}_{-2.8}$
$R_{C,h1}$ ($''$)	6.7	$^{+0.7}_{-0.9}$	$^{+1.4}_{-1.8}$	$^{+2.1}_{-2.5}$
$\sigma_{0,h1}$ (km s^{-1})	707	$^{+23}_{-23}$	$^{+45}_{-51}$	$^{+64}_{-83}$
x_{h2} ($''$)	19.9	$^{+0.3}_{-0.3}$	$^{+0.8}_{-0.7}$	$^{+1.6}_{-1.1}$
y_{h2} ($''$)	−37.0	$^{+0.6}_{-0.6}$	$^{+1.3}_{-1.4}$	$^{+1.9}_{-2.6}$
ϵ_{h2}	0.77	$^{+0.01}_{-0.01}$	$^{+0.03}_{-0.03}$	$^{+0.04}_{-0.05}$
θ_{h2} (degree)	126.1	$^{+0.4}_{-0.4}$	$^{+0.8}_{-0.9}$	$^{+1.3}_{-1.3}$
$R_{C,h2}$ ($''$)	12.5	$^{+0.6}_{-0.7}$	$^{+1.2}_{-1.5}$	$^{+1.9}_{-2.2}$
$\sigma_{0,h2}$ (km s^{-1})	1064	$^{+16}_{-17}$	$^{+31}_{-37}$	$^{+49}_{-63}$
x_{h3}($''$)	−34.4	$^{+0.9}_{-1.1}$	$^{+1.9}_{-2.6}$	$^{+2.7}_{-4.6}$
y_{h3} ($''$)	8.1	$^{+1.0}_{-0.7}$	$^{+2.7}_{-1.4}$	$^{+4.3}_{-2.0}$
$R_{C,\ h3}$ ($''$)	4.4	$^{+2.4}_{-2.2}$	$^{+4.8}_{-3.8}$	$^{+7.4}_{-4.3}$
$\sigma_{0,h3}$ (km s^{-1})	350	$^{+51}_{-48}$	$^{+104}_{-84}$	$^{+167}_{-107}$
$R_{T,\ g}$ ($''$)	7.8	$^{+2.3}_{-1.5}$	$^{+7.7}_{-3.4}$	$^{+12,6}_{-4.5}$
$\sigma_{0,g}$ (km s^{-1})	318	$^{+11}_{-74}$	$^{+42}_{-101}$	$^{+67}_{-121}$

Note. The center position refers to the northeast BCG, G1 (R.A. = 04:16:09.154 and decl. = −24:04:02.90). The angles θ_{h1} and θ_{h2} are measured counterclockwise from the west axis.

5. Discussion

To compare the results of the different clusters in a consistent way, we decide to rescale the values of their masses, surface mass densities, and radii. To do this, we use the values of the mass M_{200c} and of the corresponding radius R_{200c}, derived by Umetsu et al. (2014) via a weak-lensing shear-and-magnification

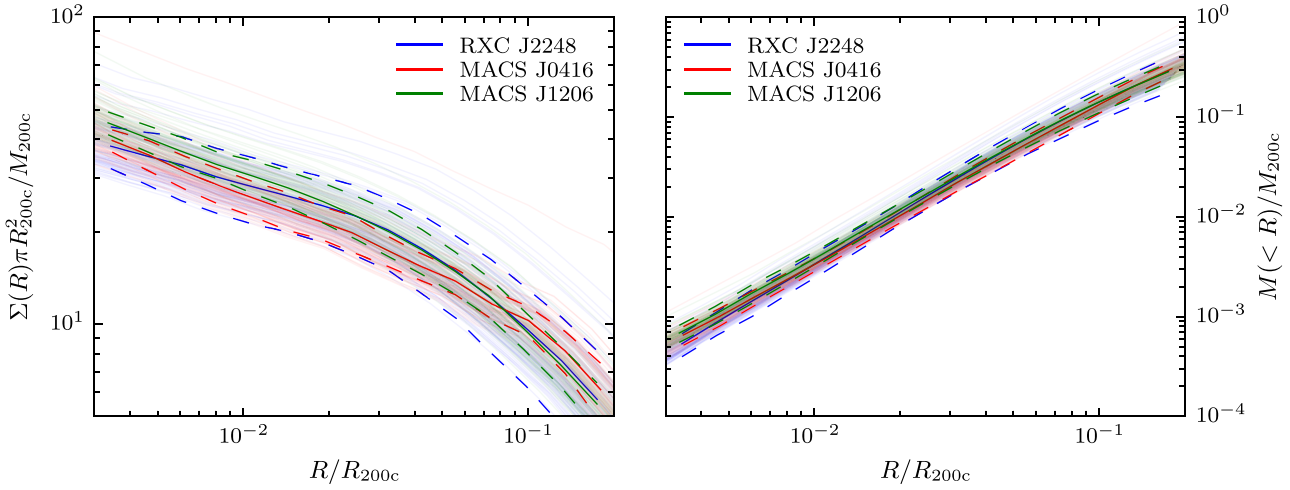

Figure 4. Normalized radial profiles of the total surface mass density (left-hand panel) and cumulative projected mass (right-hand panel) of RXC J2248 (blue), MACS J0416 (red) and MACS J1206 (green). Thin lines show a subsample of the posterior distribution, while solid and dashed lines show the mean and standard deviation.

Table 7
MACS J1206: Median Values and Confidence Level (CL) Uncertainties for the Strong-lensing Model Parameters

	Median	68% CL	95% CL	99.7% CL
x_{h1} ($''$)	−0.9	$^{+0.4}_{-0.5}$	$^{+0.8}_{-1.0}$	$^{+1.2}_{-1.4}$
y_{h1} ($''$)	0.3	$^{+0.2}_{-0.3}$	$^{+0.4}_{-0.5}$	$^{+0.6}_{-0.8}$
ϵ_{h1}	0.69	$^{+0.03}_{-0.03}$	$^{+0.05}_{-0.05}$	$^{+0.08}_{-0.09}$
θ_{h1} (degree)	19.7	$^{+0.9}_{-0.8}$	$^{+1.8}_{-1.7}$	$^{+2.7}_{-2.6}$
$R_{C,h1}$ ($''$)	6.7	$^{+0.5}_{-0.5}$	$^{+1.2}_{-1.1}$	$^{+2.4}_{-1.6}$
$\sigma_{0,h1}$ (km s^{-1})	968	$^{+41}_{-46}$	$^{+95}_{-98}$	$^{+182}_{-146}$
x_{h2}($''$)	9.5	$^{+0.8}_{-0.7}$	$^{+1.8}_{-1.4}$	$^{+2.9}_{-2.1}$
y_{h2} ($''$)	4.0	$^{+0.7}_{-0.7}$	$^{+1.5}_{-1.8}$	$^{+2.4}_{-3.8}$
ϵ_{h2}	0.55	$^{+0.10}_{-0.11}$	$^{+0.20}_{-0.21}$	$^{+0.32}_{-0.30}$
θ_{h2} (degree)	115.1	$^{+3.0}_{-2.4}$	$^{+6.5}_{-4.5}$	$^{+10.3}_{-6.4}$
$R_{C,h2}$ ($''$)	13.9	$^{+1.5}_{-1.1}$	$^{+3.4}_{-2.0}$	$^{+6.1}_{-2.8}$
$\sigma_{0,h2}$ (km s^{-1})	758	$^{+37}_{-36}$	$^{+79}_{-79}$	$^{+123}_{-147}$
x_{h3} ($''$)	−28.6	$^{+1.4}_{-1.7}$	$^{+2.8}_{-5.1}$	$^{+4.2}_{-26.2}$
y_{h3} ($''$)	−6.7	$^{+0.9}_{-0.8}$	$^{+2.8}_{-1.6}$	$^{+7.6}_{-2.5}$
ϵ_{h3}	0.35	$^{+0.06}_{-0.06}$	$^{+0.13}_{-0.13}$	$^{+0.19}_{-0.20}$
θ_{h3} (degree)	−25.4	$^{+10.2}_{-11.6}$	$^{+18.0}_{-22.5}$	$^{+24.0}_{-33.7}$
$R_{C,h3}$ ($''$)	12.3	$^{+2.3}_{-2.1}$	$^{+5.1}_{-4.0}$	$^{+14.1}_{-6.1}$
$\sigma_{0,h3}$ (km s^{-1})	600	$^{+45}_{-41}$	$^{+97}_{-84}$	$^{+157}_{-159}$
γ_4	0.11	$^{+0.01}_{-0.01}$	$^{+0.02}_{-0.02}$	$^{+0.03}_{-0.03}$
θ_4 (degree)	101.5	$^{+1.5}_{-1.4}$	$^{+3.0}_{-3.4}$	$^{+4.8}_{-6.8}$
$R_{T,g}$ ($''$)	3.6	$^{+0.9}_{-0.7}$	$^{+1.9}_{-1.4}$	$^{+3.2}_{-2.0}$
$\sigma_{0,g}$ (km s^{-1})	353	$^{+24}_{-21}$	$^{+53}_{-40}$	$^{+93}_{-57}$

Note. The center position refers to the BCG (R.A. = 2:06:12.149 and decl. = −8:48:03.37). The angles θ_{h1}, θ_{h2}, θ_{h3}, and θ_4 are measured counterclockwise from the west axis. The parameters γ_4 and θ_4 are the shear and its angle.

respectively. The thin lines represent a subsample of the models extracted from the sampling, while the solid and dashed lines show the mean and standard deviation. In these and the following figures, we have identified each cluster with a different color: blue for RXC J2248, red for MACS J0416 and green for MACS J1206. Even though these measurements are dominated by the errors on the total mass and radius from the weak-lensing analysis, the differences between the three clusters are small, both in terms of density and enclosed mass, which suggests the existence of a homologous mass profile. In Appendix C, we fit these profiles with Navarro–Frenk–White (NFW) profiles (Navarro et al. 1997) and discuss the caveats of claiming the universality of mass profiles that are fitted in projection. It should be noted that this remarkably good agreement between the rescaled mass profiles was not expected a priori: the values of M_{200c} have been measured at much larger scales ($R \sim R_{200c}$) through weak lensing (Umetsu et al. 2014), while the current analysis is restricted only to the cores of the clusters ($R < 0.2R_{200c}$). Previous works (Biviano et al. 2013; Grillo et al. 2015; Balestra et al. 2016; Caminha et al. 2017b) have shown that in these clusters with high-quality data, the results of different mass diagnostics, where they overlap, agree very well.

Using the surface mass densities of the different cluster components (from Figure 2), we can create maps of the diffuse DM and hot gas over total mass fractions. These are shown, respectively, on the left-hand and right-hand panel of Figure 5. While the galaxy clusters MACS J0416 and MACS J1206 have comparable fractions of DM, with similar trend with the radial distance from the center, RXC J2248 has a lower DM fraction and a much steeper radial dependence. Moreover, the alignment of the DM fraction isocontours seems to be perpendicular to the orientation of the cluster. This apparent misalignment is due to a combination of multiple factors. First, the difference in shape between the DM and hot gas mass distributions causes the DM to become less dominant along the direction perpendicular to its mass distribution major axis. Although less pronounced, this effect can also be seen in MACS J0416. Second, the offset between the gas and DM components causes the southeast region to have less hot gas and, therefore, a larger DM mass fraction. Moreover, these effects are increased by the larger truncation radii of the cluster-member galaxies, $R_{T,g}$, that extend their influence in the total mass budget. Meanwhile, the hot gas over total mass fraction maps are more consistent between the clusters, with their centers having lower fractions than the outskirts. However, the

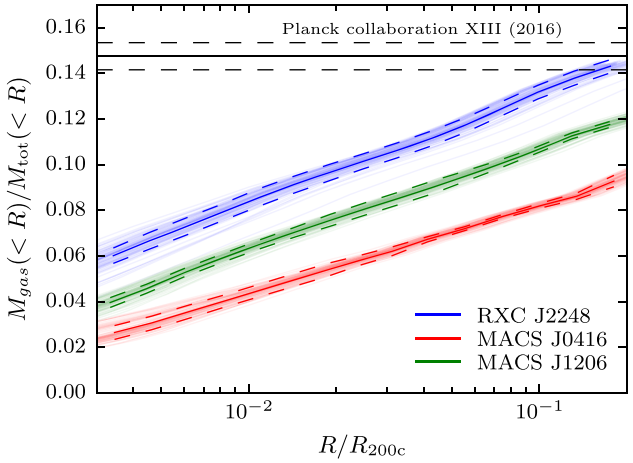

Figure 6. Ratios of the cumulative projected hot gas and total mass for RXC J2248 (blue), MACS J0416 (red) and MACS J1206 (green). The thin lines show a subsample of the posterior distribution, while the solid and dashed lines show the mean and standard deviation.

mass component of RXC J2248 and MACS J1206. Noticeably, we are able to measure the hot gas fraction with very high precision, (less than 1% before rescaling), thanks to the small uncertainties on the cluster total mass derived from our high-precision strong-lensing models.

Finally, expanding the analysis by Grillo et al. (2015) and Munari et al. (2016), we look at the substructure statistics in the three clusters, traced by their member galaxies. We compare our measurements, derived from the new strong-lensing model (Section 2.2), to those presented by Grillo et al. (2015), both on the observed data of MACS J0416 and the simulated halos. To increase the statistics, we consider here simulated (N-body) halos that have M_{200c} values larger than $9 \times 10^{14} M_{\odot}$ from four snapshots, at the following redshifts: 0.25, 0.28, 0.46 and 0.51. In all of the clusters, we select only those galaxies, or sub-halos, that have a circular velocity value $v_c = \sqrt{2}\,\sigma_0$ larger than 90 km s^{-1} and which are located within a projected distance of $0.16 \times R_{200c}$ from the cluster centers. Compared to the previous studies, we change these velocity and projected distance limits to better compare clusters with different masses and to avoid the mass resolution limit that would otherwise contaminate the results at the low circular velocity end for the simulated sub-halos. We refer to the original papers for any other details on the strong-lensing model and simulated data. We then compute the galaxy radial number distribution and circular velocity distribution, as shown in the left-hand and right-hand panels of Figure 7. Moreover, in Figure 8, we show the circular velocity function of the member galaxies; i.e., the fraction of member galaxies with circular velocity larger than the considered value. In both plots, the points with error bars mark the median and 16th–84th percentiles, computed from a sample of models extracted from the MCMC sampling. The gray-shaded areas represent the values obtained from numerical simulations, as presented by Grillo et al. (2015). In Figure 7, we also show the observed data from Grillo et al. (2015). The color scheme is the same as in the previous plots. Interestingly, the circular velocity function of the cluster members of MACS J1206 is more similar to that of MACS J0416, a merging cluster, than to that of RXC J2248, a relaxed cluster. In their work, Grillo et al. (2015) noticed how the number of massive substructures ($v_c > 100$ km s^{-1}) is underestimated in numerical simulations, even when baryonic effects are included (Munari et al. 2016). Similarly, we find that both in terms of radial and velocity distributions, the results presented in this work are consistent with those by Grillo et al. (2015); i.e., in tension with the predictions of numerical simulations, and partially at odds with those by Natarajan et al. (2017). Only the circular velocity function of RXC J2248 seems to be within the intrinsic scatter of the simulated data; however, in the observed cluster the number of sub-halos with a given circular velocity is still a factor of approximately three larger than that found in simulations. These differences cannot be solved by invoking possible misidentifications of cluster members because our extensive spectroscopy and 12-band CLASH photometry lead to highly pure samples (i.e., very few false positives) and the vast majority of the high-velocity cluster members are confirmed spectroscopically (see Figure 4 in Caminha et al. 2017a).

6. Conclusions

Thanks to the very high quality of the multiwavelength data available, we have been able to separate the collisional and collisionless mass components in the galaxy clusters RXC J2248.7−4431, MACS J0416.1−2403, and MACS J1206.2−0847 at $z \approx 0.4$. Two of them, RXC J2248 and MACS J0416, are part of the HFF sample (Lotz et al. 2017) and all three have been observed with both the VIMOS (CLASH-VLT program; Rosati et al. 2014) and the MUSE (archive observations) instruments at the VLT. Following the method presented by Bonamigo et al. (2017), we have modeled the hot gas mass by fitting the X-ray surface brightness from deep *Chandra* observations of the clusters. Then, we have introduced this mass term in the strong-lensing analysis as a fixed component.

The main results of the work can be summarized as follows:

1. We have provided 2D models of the hot intracluster gas mass density of these three clusters (updating that of MACS J0416) that are consistent with a well-tested and independent approach (Ettori et al. 2013) and which can be easily included in different gravitational lensing software.
2. With the decoupling of the hot gas from the other cluster mass components, we have improved previous strong-lensing models to more accurately describe the different contributions to the total mass budget of the clusters. Due to their different physical nature, the cluster hot gas and DM halo components exhibit different properties, seen both in their surface mass density maps and in their cumulative radial mass profiles.
3. The isolation of the diffuse DM component has allowed us to measure with high accuracy the absence of a significant offset between the diffuse DM density peaks and the positions of the BCGs, which is a test for models of self-interacting DM.
4. By rescaling the radial profiles of the cluster projected mass with the values of R_{200c} and M_{200c}, we have shown that these clusters manifest an almost homologous structure, despite their significantly different relaxation status.
5. By exploiting the small statistical uncertainties on the cluster total mass derived from our strong-lensing analysis, we have measured the hot gas over total mass fraction throughout the core of the clusters with

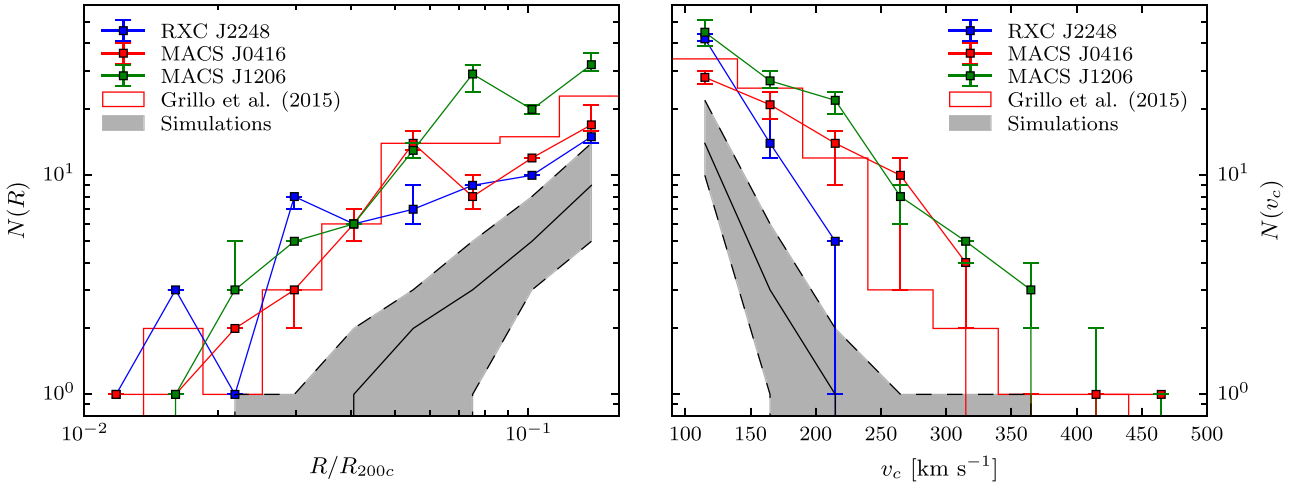

Figure 7. Radial profiles of the number density and circular velocity distributions of the member galaxies for RXC J2248 (blue), MACS J0416 (red) and MACS J1206 (green). Only galaxies within a circular aperture of $0.16 \times R_{200c}$ and with circular velocity larger than 90 km s^{-1} are considered. Points and error bars show the median and 16th–84th percentiles, respectively. Red histograms are the values derived from the model of MACS J0416 by Grillo et al. (2015), where a slightly different value for the center of the cluster was adopted.

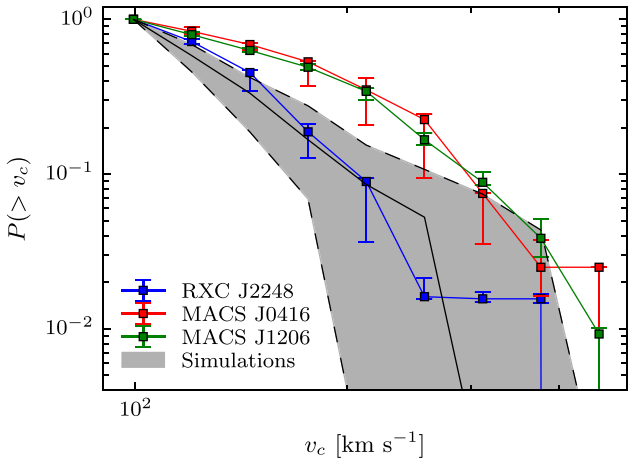

Figure 8. Circular velocity function of the member galaxies for RXC J2248 (blue), MACS J0416 (red) and MACS J1206 (green). Only galaxies within a circular aperture of $0.16 \times R_{200c}$ and with a circular velocity larger than 90 km s^{-1} are considered. Points and error bars show the median and 16th–84th percentiles, respectively.

unprecedented precision (less than 1%). A remarkable advantage of the adopted approach is the possibility of investigating spatially resolved maps of the gas fraction, in addition to the traditional radial profiles.

6. Finally, we have confirmed the findings by Grillo et al. (2015) and Munari et al. (2016) that current N-body simulations under-predict the number of massive sub-halos ($v_c > 90$ km s^{-1}) in the cores of massive clusters. This discrepancy is visible in all three clusters of our sample.

In this paper we have shown the advantages of an accurate multiwavelength study of a well-selected sample of clusters with high-quality data. Extending the sample to even more clusters and comparing the results with the outcomes of cosmological simulations will allow us to tackle some of the remaining questions about the nature of DM and the internal structure of galaxy clusters. The importance of detailed and accurate studies of galaxy clusters is clear. In this era of large all-sky surveys, the information that is gained from vast samples of galaxy clusters relies on the accuracy of the adopted priors and models. Only by testing these assumptions on a smaller, well-understood sample is it possible to push forward our knowledge of DM and the other components of the universe.

M.B. and C.G. acknowledge support by VILLUM FONDEN Young Investigator Programme through grant no. 10123. S.E. acknowledges the financial support from contracts ASI-INAF I/009/10/0, NARO15 ASI-INAF I/037/12/0 and ASI 2015-046-R.0. G.B.C. acknowledges funding from the ERC Consolidator Grant ID 681627-BUILDUP (P.I. Caputi). G.B. C., P.R., A.M., M.A. and M.L. acknowledge financial support from PRIN-INAF 2014 1.05.01.94.02. AM acknowledges funding from the INAF PRIN-SKA 2017 program 1.05.01.88.04. Simulated data postprocessing and storage has been done on the CINECA facility PICO thanks to che Iscra C grant GALPP_3.

Appendix A
Alternative Hot Gas Mass Models

When fitting the X-ray surface brightness, we model the cluster hot gas mass density distributions with either two or three components (three and four for MACS J0416), with both spherical and elliptical symmetry. The selection of the final best-fitting model is done by considering the AIC (Akaike 1974) and the BIC (Schwarz 1978). Here, we are mainly interested in the projected mass profiles of the clusters; therefore, we compare our results with independent measurements of the cumulative projected hot gas mass profiles of RXC J2248, MACS J0416, and MACS J1206. In Figure 9, the gray areas show the 1σ confidence regions of these mass profiles, while the dashed and solid lines show, respectively, the spherical- and elliptical-component models tested in this work (based on Bonamigo et al. 2017). Different colors represent models with different numbers of components, as indicated on the legends. The model used as comparison has been recovered through the geometrical deprojection (see, e.g.,

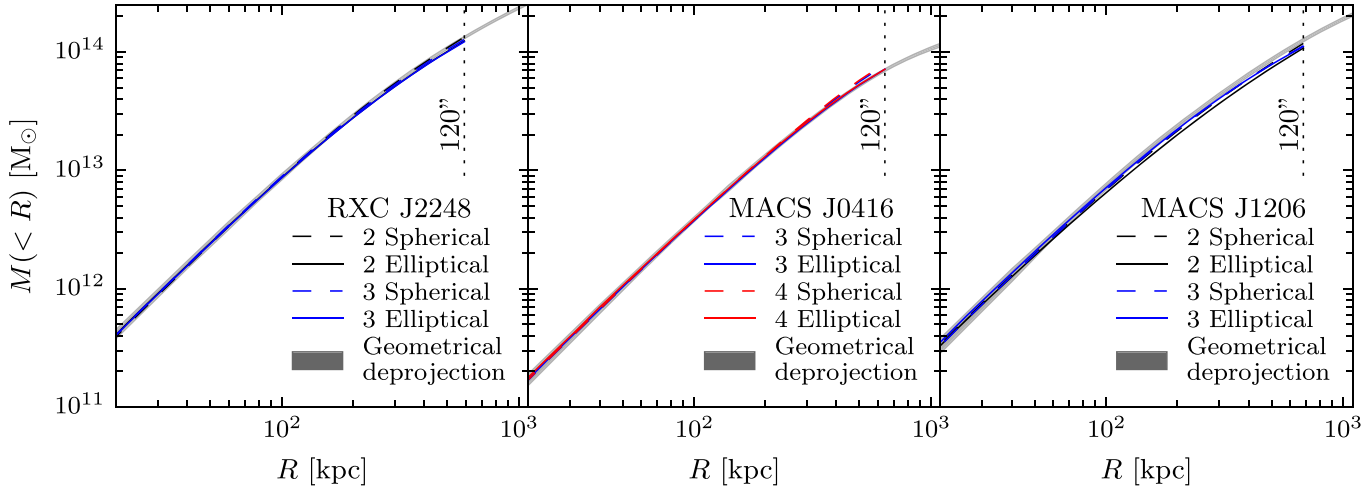

Figure 9. Cumulative projected hot gas mass profiles of RXC J2248, MACS J0416 and MACS J1206, respectively, on the left-hand, center and right-hand panel. Dashed and solid lines show, the spherical- and elliptical-component models, respectively. Black, blue and red lines refer to models with two, three and four components. The gray areas show the 1σ confidence regions of the mass profile obtained through a geometrical deprojection.

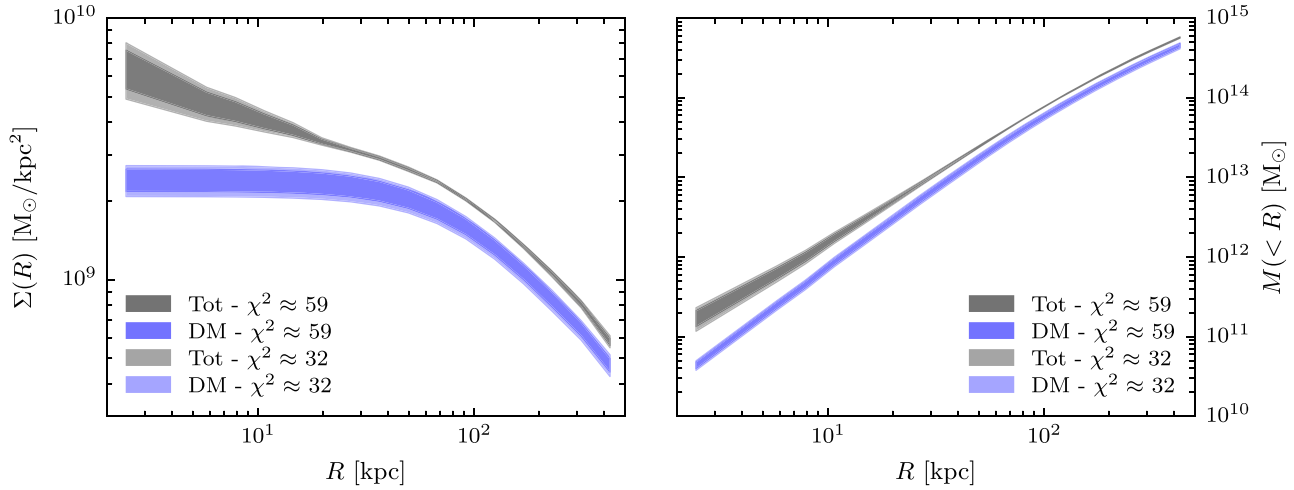

Figure 10. Radial profiles of the surface mass density (left-hand panel) and cumulative projected mass (right-hand panel) for the total (black) and dark-matter component (blue) of RXC J2248. The areas show values at the 3σ confidence level. Darker and lighter refer to values of the minimum χ^2 of approximately 59 (reference model in this work) and 32, respectively.

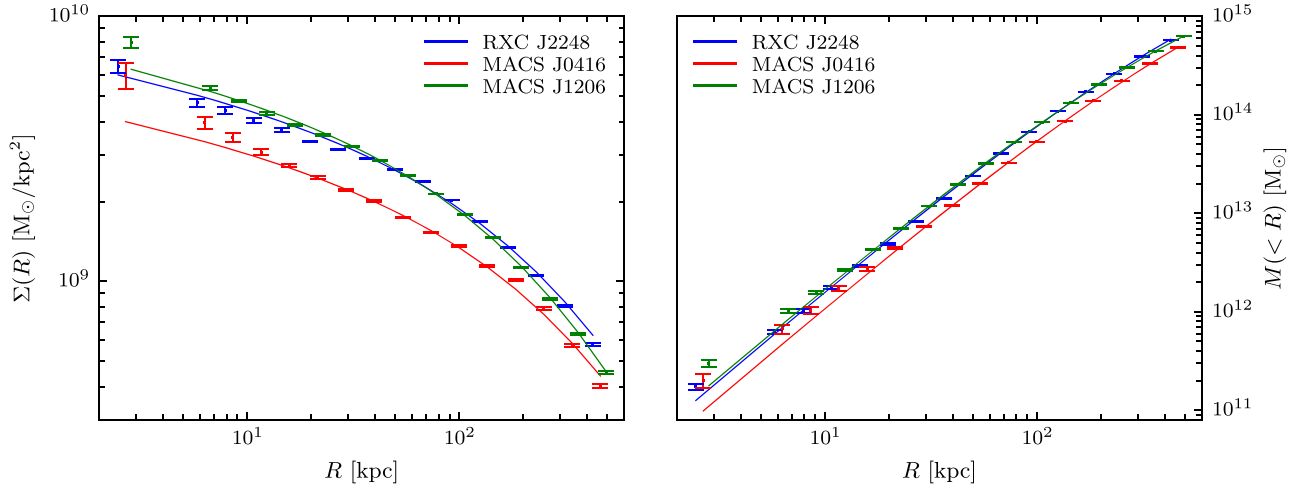

Figure 11. Radial profiles of the total surface mass density (left-hand panel) and cumulative projected mass (right-hand panel) of RXC J2248 (blue), MACS J0416 (red) and MACS J1206 (green). The data points with error bars show the fitted data, as measured from the strong-lensing analysis. The solid lines represent the best-fit NFW profiles to the data.

Ettori et al. 2013, and references therein) of the azimuthally averaged surface brightness profile that considers the entire X-ray emission of the cluster. The striking agreement with this different and independent method corroborates the accuracy of our measurements, especially in the regions of interest in the lensing analysis; i.e., $R < 400$ kpc.

Appendix B
Effect of the Intrinsic Variance of the χ^2 Distribution

As in any other distribution, the χ^2 distribution has an intrinsic variance that is a function of the model d.o.f. Because of this, even a perfect model is not guaranteed to have a value of the χ^2 equal to the number of the d.o.f. (Andrae et al. 2010). Therefore, when we require the best-fit model to have a χ^2 value that is approximately equal to the number of d.o.f., we introduce a systematic error, that propagates into the uncertainties on the mass-component parameter distributions and on the mass and density radial profiles. To better quantify this effect, we consider the value of the 0.13 percentile (99.7% CL) of the χ^2 distribution for our best-fit strong-lensing model of RXC J2248. This gives a conservative model that can be considered as an upper limit on the errors of the mass models presented in this paper. Given the 59 d.o.f. for RXC J2248, the 0.13-percentile of the corresponding χ^2 distribution is 31.7. Therefore, to investigate this more conservative model, we increase the uncertainty on the image positions to $0\farcs66$, to get a minimum chi-square value of approximately 32, while in the main-text model the error is $0\farcs48$. We then use the same procedure as presented above to compute the surface mass density and cumulative projected mass radial profiles, as shown, respectively, on the left-hand and right-hand panel of Figure 10. The filled areas represent the 3σ uncertainties on the radial profiles of the main-text (darker colors) and conservative (lighter colors) models, respectively. Black and blue areas show the total and DM-only component. We remark that the 3σ CL values of the profiles shown in Figure 10 for the two different models are very similar. The results of this test thus suggest that the variance of the χ^2 distribution does not significantly affect the final errors on the values of the parameters and of the derived quantities of the model.

Appendix C
On the Homologous Projected Profiles

As noted in Section 5, the rescaled surface density and cumulative projected mass profiles of the three clusters are very similar, suggesting the existence of a homologous mass profile. Indeed, DM-only numerical simulations have shown that the averaged mass profile of virialized halos is well-described by a universal profile, the so-called NFW profile (Navarro et al. 1997). We use a NFW profile to fit, separately, both the surface mass density and the cumulative projected mass profiles estimated in our strong-lensing analyses. The best-fitting profiles obtained from the optimized values are shown in Figure 11 as solid lines. Points with error bars show the mean and standard deviation of the measured surface mass density (left-hand panel) and cumulative projected mass (right-hand panel) that have been fitted. With the exception of the innermost regions, dominated by the BCGs, a NFW profile provides a good fit to the data, as shown in Umetsu et al. (2014) for the CLASH cluster sample. We remark that the data points are obtained from the combination of multiple components, described by different (cored) isothermal mass profiles, which are favored over the NFW profiles by the strong-lensing analyses, as shown in Grillo et al. (2015) and Caminha et al. (2017b) for MACS J0416 and MACS J1206, respectively. This suggests that other one-component models, with a varying radial slope, might also provide good fits to the reconstructed profiles of the clusters in their cores when they are considered in projection. We believe that the best way to distinguish among the different models is to use the chi-square statistics directly on the difference between the observed and model-predicted positions of the multiple images and that a good fit on the reconstructed projected quantities of a complex astrophysical object might not be enough to state the definite success of a particular model.

ORCID iDs

M. Bonamigo https://orcid.org/0000-0002-1461-1115
C. Grillo https://orcid.org/0000-0002-5926-7143
S. Ettori https://orcid.org/0000-0003-4117-8617
G. B. Caminha https://orcid.org/0000-0001-6052-3274
A. Mercurio https://orcid.org/0000-0001-9261-7849
I. Balestra https://orcid.org/0000-0001-9660-894X
M. Lombardi https://orcid.org/0000-0002-3336-4965

References

Abell, G. O., Corwin, H. G., Jr., & Olowin, R. P. 1989, ApJS, 70, 1
Acebron, A., Jullo, E., Limousin, M., et al. 2017, MNRAS, 470, 1809
Akaike, H. 1974, ITAC, 19, 716
Allen, S. W., Rapetti, D. A., Schmidt, R. W., et al. 2008, MNRAS, 383, 879
Andrae, R., Schulze-Hartung, T., & Melchior, P. 2010, arXiv:1012.3754
Annunziatella, M., Bonamigo, M., Grillo, C., et al. 2018, ApJ, 851, 81
Bacon, R., Accardo, M., Adjali, L., et al. 2012, Msngr, 147, 4
Balestra, I., Mercurio, A., Sartoris, B., et al. 2016, ApJS, 224, 33
Balestra, I., Vanzella, E., Rosati, P., et al. 2013, A&A, 559, L9
Bender, R., Burstein, D., & Faber, S. M. 1992, ApJ, 399, 462
Biviano, A., Rosati, P., Balestra, I., et al. 2013, A&A, 558, A1
Böhringer, H., Schuecker, P., Guzzo, L., et al. 2001, A&A, 369, 826
Bonamigo, M., Grillo, C., Ettori, S., et al. 2017, ApJ, 842, 132
Caminha, G. B., Grillo, C., Rosati, P., et al. 2016, A&A, 587, A80
Caminha, G. B., Grillo, C., Rosati, P., et al. 2017a, A&A, 600, A90
Caminha, G. B., Grillo, C., Rosati, P., et al. 2017b, A&A, 607, A93
Chirivì, G., Suyu, S. H., Grillo, C., et al. 2018, A&A, 614, A8
Clowe, D., Bradač, M., Gonzalez, A. H., et al. 2006, ApJL, 648, L109
Donahue, M., Voit, G. M., Mahdavi, A., et al. 2014, ApJ, 794, 136
Ettori, S. 2000, MNRAS, 311, 313
Ettori, S., Donnarumma, A., Pointecouteau, E., et al. 2013, SSRv, 177, 119
Ettori, S., Tozzi, P., & Rosati, P. 2003, A&A, 398, 879
Evrard, A. E. 1997, MNRAS, 292, 289
Faber, S. M., Dressler, A., Davies, R. L., Burstein, D., & Lynden-Bell, D. 1987, in Proc. of the Eighth Santa Cruz Summer Workshop in Astronomy and Astrophysics, Nearly Normal Galaxies. From the Planck Time to the Present, ed. S. M. Faber (New York: Springer), 175
Firmani, C., D'Onghia, E., Avila-Reese, V., Chincarini, G., & Hernández, X. 2000, MNRAS, 315, L29
Grillo, C., Karman, W., Suyu, S. H., et al. 2016, ApJ, 822, 78
Grillo, C., Suyu, S. H., Rosati, P., et al. 2015, ApJ, 800, 38
Jullo, E., Kneib, J.-P., Limousin, M., et al. 2007, NJPh, 9, 447
Karman, W., Caputi, K. I., Caminha, G. B., et al. 2017, A&A, 599, A28
Kassiola, A., & Kovner, I. 1993, ApJ, 417, 450
Kawamata, R., Ishigaki, M., Shimasaku, K., et al. 2018, ApJ, 855, 4
Lagattuta, D. J., Richard, J., Clément, B., et al. 2017, MNRAS, 469, 3946
Elíasdóttir, Á., Limousin, M., Richard, J., et al. 2007, arXiv:0710.5636
Lotz, J. M., Koekemoer, A., Coe, D., et al. 2017, ApJ, 837, 97
Macciò, A. V., Paduroiu, S., Anderhalden, D., Schneider, A., & Moore, B. 2012, MNRAS, 424, 1105
Mahler, G., Richard, J., Clément, B., et al. 2018, MNRAS, 473, 663
Mann, A. W., & Ebeling, H. 2012, MNRAS, 420, 2120
Monna, A., Seitz, S., Balestra, I., et al. 2017, MNRAS, 466, 4094

Morandi, A., Limousin, M., Sayers, J., et al. 2012, MNRAS, 425, 2069
Munari, E., Grillo, C., De Lucia, G., et al. 2016, ApJL, 827, L5
Natarajan, P., Chadayammuri, U., Jauzac, M., et al. 2017, MNRAS, 468, 1962
Navarro, J. F., Frenk, C. S., & White, S. D. M. 1997, ApJ, 490, 493
Ogrean, G. A., van Weeren, R. J., Jones, C., et al. 2016, ApJ, 819, 113
Planck Collaboration, Ade, P. A. R., Aghanim, N., et al. 2016, A&A, 594, A13
Planelles, S., Borgani, S., Dolag, K., et al. 2013, MNRAS, 431, 1487
Postman, M., Coe, D., Benítez, N., et al. 2012, ApJS, 199, 25
Richard, J., Patricio, V., Martinez, J., et al. 2015, MNRAS, 446, L16
Rosati, P., Balestra, I., Grillo, C., et al. 2014, Msngr, 158, 48
Rumsey, C., Olamaie, M., Perrott, Y. C., et al. 2016, MNRAS, 460, 569
Salmon, B., Coe, D., Bradley, L., et al. 2017, arXiv:1710.08930
Schwarz, G. 1978, AnSta, 6, 461
Sereno, M., Ettori, S., Meneghetti, M., et al. 2017, MNRAS, 467, 3801
Spergel, D. N., & Steinhardt, P. J. 2000, PhRvL, 84, 3760
Suyu, S. H., & Halkola, A. 2010, A&A, 524, A94
Umetsu, K., Medezinski, E., Nonino, M., et al. 2014, ApJ, 795, 163
Umetsu, K., Sereno, M., Medezinski, E., et al. 2015, ApJ, 806, 207
van Weeren, R. J., Ogrean, G. A., Jones, C., et al. 2017, ApJ, 835, 197
Vogelsberger, M., Zavala, J., & Loeb, A. 2012, MNRAS, 423, 3740
Wechsler, R. H., Bullock, J. S., Primack, J. R., Kravtsov, A. V., & Dekel, A. 2002, ApJ, 568, 52
White, S. D. M., Navarro, J. F., Evrard, A. E., & Frenk, C. S. 1993, Natur, 366, 429
Zhao, D. H., Mo, H. J., Jing, Y. P., & Börner, G. 2003, MNRAS, 339, 12
Zitrin, A., Rosati, P., Nonino, M., et al. 2012, ApJ, 749, 97